International Journal of Minerals, Metallurgy and Materials
Volume 26, Number 7, July 2019, Page 869
https://doi.org/10.1007/s12613-019-1799-4

Effect of heat treatment on the microstructure and micromechanical properties of the rapidly solidified $Mg_{61.7}Zn_{34}Gd_{4.3}$ alloy containing icosahedral phase

Wen-bo Luo[1,2], *Zhi-yong Xue*[2,3], *and Wei-min Mao*[1]

1) School of Materials Science and Engineering, University of Science and Technology Beijing, Beijing 100083, China
2) Institute for Advanced Materials, North China Electric Power University, Beijing 102206, China
3) School of Energy, Power and Mechanical Engineering, North China Electric Power University, Beijing 102206, China
(Received: 5 September 2018; revised: 7 January 2019; accepted: 11 January 2019)

Abstract: In this paper, the microstructure evolution of the rapidly solidified (RS) $Mg_{61.7}Zn_{34}Gd_{4.3}$ (at%, atomic ratio) alloy at high temperatures was investigated. The hardness and elastic modulus of the main precipitated phases were also analyzed and compared with those of the α-Mg matrix on the basis of nanoindentation tests. The results show that the RS alloy consists of either a petal-like icosahedral quasicrystal (IQC) phase (~20 μm) and block-shaped H1 phase (~15 μm) or IQC particles with an average grain size of ~107 nm as well as a small proportion of amorphous phase, which mainly depends on the holding time at the liquid temperature and the thickness of the ribbons. The IQC phase gradually transforms at 400°C to a short-rod-shaped μ-phase ($Mg_{28.6}Zn_{63.8}Gd_{7.7}$) with a hexagonal structure. The hardness of the IQC phase is higher than that of H1 phase, and both phases exhibit a higher hardness than the α-Mg matrix and the μ-phase. The elasticity of the H1 phase is superior to that of the α-Mg matrix. The IQC phase possesses a higher elastic modulus than H1 phase. The easily formed H1 phase exhibits the poorest plastic deformation capacity among these phases but a higher elastic modulus than the α-Mg matrix.

Keywords: magnesium alloy; icosahedral phase; rapidly solidification; nanoindentation; micromechanical properties

1. Introduction

With increasing emphasis on reducing weight in the aircraft field, Mg alloys are attracting attention for their lightweight character and excellent castability [1–2]. Because of their outstanding mechanical properties and corrosion resistance, Mg–RE (RE denotes a rare-earth element) series alloys have become representative high-performance Mg alloys [3–4]. These Mg alloys contain some special but significant strengthening phases, one of which is the icosahedral quasicrystal (IQC) phase [5–6].

The IQC phase has received intensive attention because it exhibits higher hardness and better wear resistance than most of the strengthening phases in commercial Mg alloys [7]. As a three-dimensional quasicrystal structure, the atom-cluster structure of the IQC phase belongs to the Samson–Pauling–Bergman model (a triacontahedron structure) [8–9]. In the past few decades, numerous IQC phases have been found and investigated, including $Mg_{32}(Zn, Al)_{49}$ [10], $Mg_{35}Al_{49}Ag_{15}$, and $Mg_{30}Zn_{60}RE_{10}$ [11]. Such phases are also commonly added to other Mg alloys with free-RE elements to enhance their strength [12–13]. For example, when the Mg_3Zn_6Gd (at%) IQC phase was introduced into AZ31 alloy via a mechanical process, the tensile yield strength of the alloy reached 334 MPa [14]. Recently, stable IQC-phase-based Mg–Zn–RE and Mg–Zn–Sc have been developed and studied [15], but the thermal stability of the IQC phase is uncertain [16]. The literature contains numerous accounts of an IQC phase transformation at 400°C in Mg–Zn–RE alloys. For instance, it can transform to the hexagonal-structured H phase, the H1 phase, or even the cubic W phase [4,16–17]. However, these phases' mechanical properties are rarely discussed even though the phase transitions have been investigated in detail. The Young's elastic modulus of the ico-

Corresponding author: Wei-min Mao E-mail: mao_wm@ustb.edu.cn

sahedral Al-based alloys has been determined to be approximately 200 GPa at room temperature [7], which is substantially higher than that of Al-based alloys. However, the data for the icosahedral Mg-based alloys have seldom been reported, primarily because of the difficulty associated with preparing a bulk single crystal of the IQC-phase-based Mg–Zn–RE and its corresponding structure-approximate phases. Therefore, the mechanical properties of these phases, such as the elastic modulus and the hardness, have seldom been investigated even though they are important for the development of new Mg alloys.

The nanoindentation technique has been used to test the micromechanical properties of materials, especially thin-film materials and small-sized bulk metal glasses [18]. It has also been used to test the hardness and the modulus of the different phases in an alloy [19] because the curve of the load–depth is easily obtained [20]. In addition, various methods-based mechanical models and energy methods can be used to analyze the mechanical properties and the plastic deformation behaviors of the tested materials [21–22].

In this work, an Mg–Zn–Gd alloy was first melted and cast and then sprayed to obtain rapidly solidified (RS) ribbons with different thicknesses. The ribbons consist of plentiful nanosized IQC grains and a small proportion of amorphous phase. This paper mainly describes the microstructures of the alloy and their evolution during the heat treatment processes and examines the precipitated phases' mechanical properties on the basis of nanoindentation tests.

2. Experimental

An ingot with a nominal composition of $Mg_{61.7}Zn_{34}Gd_{4.3}$ (at%, atomic ratio) was produced from commercial pure Mg (99.98wt%, weight ratio), pure Zn (99.98wt%), and Mg–30Gd (wt%) alloy. The ingot was then melted and sprayed to obtain RS ribbons with a single copper roller spinning method, where the speed of the copper roller was approximately 20 m/s. To obtain a greater proportion of icosahedral phase, both appropriate chemical compositions and the proper techniques are needed. In the RS process, we found that both the temperature of the alloy liquid and the holding time at this temperature strongly affected the phase formation of the ribbons, especially the formation of the IQC phase. According to Ref. [23], a longer holding time at the melting temperature of an alloy favors the formation of a block-shaped IQC phase. Therefore, two kinds of processes were conducted in this work: one process conducted at a slightly lower melting power (~20 kW) and shorter holding time (3–5 s) led to thinner ribbons (50–90 μm), and the other process at a higher melting power (20–30 kW) and longer holding time (5–10 s) led to thicker ribbons (80–120 μm). Most of the as-sprayed ribbons were then subjected to an isothermal heat treatment at 400°C for 5–30 min under an Ar atmosphere. Other ribbons were subjected to a non-isothermal treatment, where the temperature was increased from RT to 400°C (heating rate of ~25°C/min) and held at 400°C for 30 min under an Ar atmosphere.

Nanoindentation tests were performed with a Nano Indenter XP tester equipped with a Berkovich tip (the elastic modulus (E_i) and the Poisson's ratio (ν_i) of the tip are about 1.141 GPa and 0.07, respectively). It recorded the displacement as a function of applied load with a high load resolution (50 nN) and a high displacement resolution (0.01 nm). The measurement parameters were as follows: maximum depth h_{max} = 1000 nm, Poisson's ratio ν = 0.35. To remove the size effects of nanoindentation, the indentation depth was unified (1000 nm) in this work. Each phase was measured at least five times to obtain the average value of the hardness and the Young's elastic modulus at room temperature and 400°C.

The phases in the alloy were identified by X-ray diffraction (XRD) (Rigaku Ultima IV 3KW, Cu-Kα radiation, at 40 kV and 300 mA); the 2θ range was from 10° to 90° with a scanning rate of $0.02°\cdot s^{-1}$. A Zeiss Auriga-EVO 18 field-emission scanning electron microscope equipped with an energy-dispersive X-ray spectroscopy (EDS) system was used to analyze the microstructure of the alloy. In addition, a Tecnai G2 F30 transmission electron microscope equipped with a high-resolution transmission electron microscopy system was also used to observe the microstructure of the phases and to analyze the parameters of the crystal lattice. Samples for scanning electron microscopy (SEM) were etched in a solution of 4vol% nitrate alcohol to reveal grain boundaries. The foils for transmission electron microscopy (TEM) observation were first mechanically polished to ~50 μm, punched into discs 3 mm in diameter, and then ion-milled using a Gatan plasma ion polisher.

3. Results and discussion

3.1. Microstructure evolution of the alloy at high temperatures

Fig. 1 shows the XRD patterns of the as-cast and RS $Mg_{61.7}Zn_{34}Gd_{4.3}$ alloy. Substantially different phases exist in the as-cast sample and the RS ribbons. Because of the high Zn and RE Gd contents (the total content of Zn and Gd is ~38.3at%), the XRD peaks of the as-cast alloy are complicated and three phases are detected in the as-cast sample:

α-Mg solid solution, Mg_7Zn_3, and the τ phase. The composition of the alloy is $Mg_{59}Zn_{35}Gd_6$, as verified by EDS in Fig. 2(d). For the RS ribbons, the XRD patterns are relatively simple and show substantial line broadening due to the formation of ultrafine crystal grains in a rapid solidification process. Notably, the IQC phase is the main second phase in the as-sprayed material. The μ-phase precipitates upon heat treatment of the ribbon at 400°C for 0.5 h. In the meantime, the intensity of the XRD peaks of the IQC phase decrease slightly. The results also show that a few particles of the Mg_7Zn_3 phases form during the non-isothermal treatment process.

Fig. 2 shows SEM images of the $Mg_{61.7}Zn_{34}Gd_{4.3}$ alloy under different conditions. For the as-cast sample (Fig. 2(a)), four precipitated phases are detected by EDS (Fig. 2(d)): the τ phase and the Mg_7Zn_3 phase were confirmed by XRD (Fig. 1), and the other two phases were analyzed as follows. One of them is confirmed to be the H1 phase (symbol A3 in Fig. 2(a)), which mainly locates on block-shaped phases; the second one is the binary MgZn phase (symbol A4 in Fig. 2(a)), which is distributed on the adjacent zone of the τ phase and the Mg_7Zn_3 phase. With regard to the RS ribbons (Figs. 2(b) and 2(c)), the main second phases are the IQC phase and the block-shaped H1 phase. On the basis of the quantitative metallographic technique, the contents of these two phases are determined to be approximately 3.4vol% and 5.5vol%, respectively. We observed that the IQC phase displays two substantially different morphologies in the RS alloy: a petal-like morphology with an average grain size of ~20 μm and fine nanosized particles with an average size of ~107 nm, as shown in Figs. 2(c) and 3(a). The irregular block-shaped H1 phase with an average grain size of ~15 μm forms directly during the solidification process in the thicker RS ribbons.

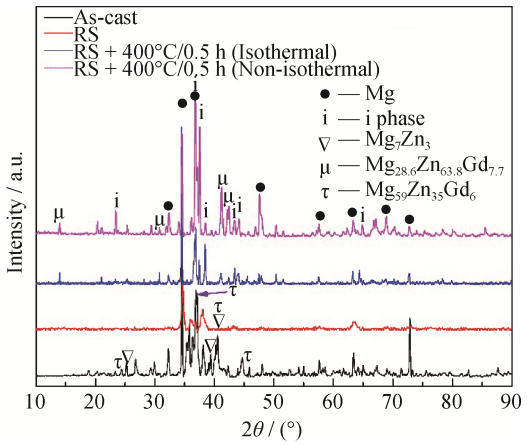

Fig. 1. XRD patterns of the $Mg_{61.7}Zn_{34}Gd_{4.3}$ alloy under various conditions.

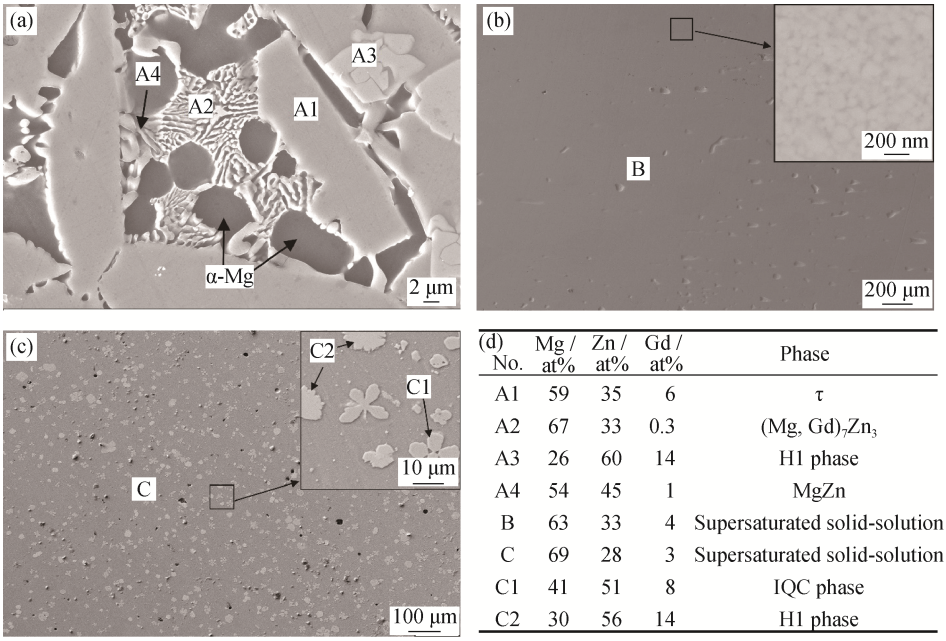

(d) No.	Mg / at%	Zn / at%	Gd / at%	Phase
A1	59	35	6	τ
A2	67	33	0.3	$(Mg, Gd)_7Zn_3$
A3	26	60	14	H1 phase
A4	54	45	1	MgZn
B	63	33	4	Supersaturated solid-solution
C	69	28	3	Supersaturated solid-solution
C1	41	51	8	IQC phase
C2	30	56	14	H1 phase

Fig. 2. SEM images and EDS analysis results of the $Mg_{61.7}Zn_{34}Gd_{4.3}$ alloy: (a) SEM image of the as-cast sample; (b,c) SEM images of the microstructure of the RS ribbons with thinner and thicker thicknesses, respectively; (d) the average EDS results of the phases in the alloy.

Fig. 3(a) shows the TEM images of both the nano-IQC phase and the amorphous phase, and no obvious other second phases are observed. The IQC particles, whose sizes range from 40 to 230 nm, show an approximately globular shape and are homogenously distributed in the RS ribbons. The volume ratio of the amorphous phase is

9vol%–21vol% in the ribbons: more amorphous phases are present in the thinner ribbon than in the thicker one. Fig. 3(b) shows a high-resolution TEM image of the small proportion of the IQC phase and the adjacent amorphous phase. It reveals that the amorphous phase has crystallized to a quasicrystalline structure to a certain extent. Figs. 3(c) and 3(d) show the selected-area electron diffraction (SAED) patterns of the nanosized IQC particles and the amorphous phase. Fig. 3(e) indicates that the IQC phase belongs to the P-type quasicrystal. Fig. 3(f) and 3(g) shows the EDS spectra of these two phases; the spectra reflect the significant differences in the chemical compositions between the intergranular amorphous region and the granular IQC phases.

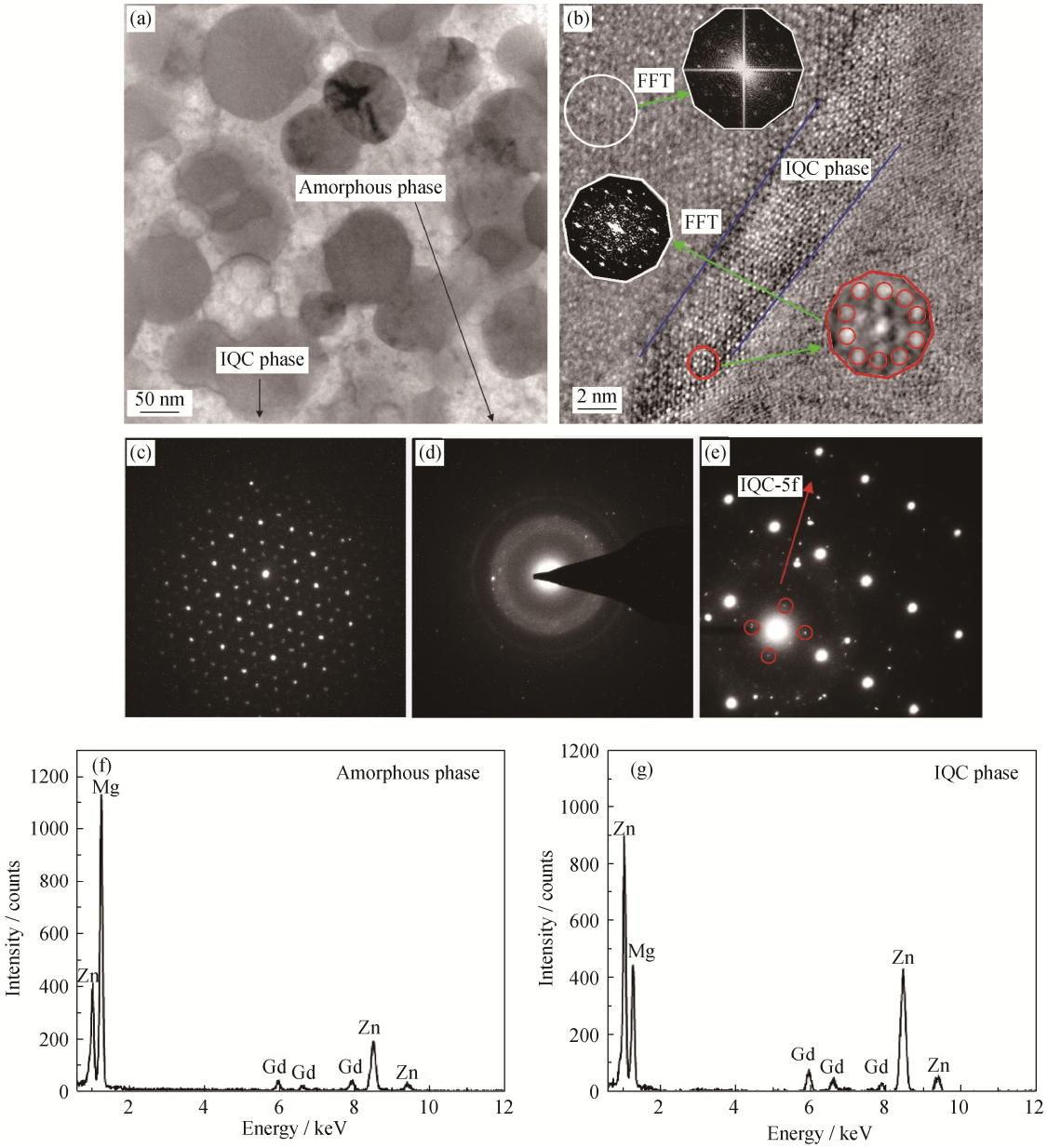

Fig. 3. TEM images, corresponding SAED patterns, and EDS spectra of the thinner RS ribbon: (a) bright-field TEM image of the nanosized IQC phase and the amorphous phase; (b) a high-resolution TEM image of the two phases, where the insets display the fast Fourier transform patterns; (c, d) the SAED patterns of the nano-IQC phase (the beam is parallel to the 5-fold axis) and the amorphous phase, respectively; (e) the SAED patterns of nano-IQC along the 2-fold axis; (f, g) EDS spectra of the amorphous phase and the IQC phase, respectively.

The atomic structure of the amorphous phase is random in the long-range and medium-range atomic environments. Some representatively atomic models of short-range order and even medium-range order have been proposed to ex-

plain the amorphous structure in recent years [24]. One of the structural models is based on icosahedral atomic stacking, where the icosahedral nuclei are speculated to already exist in the amorphous phase [7,24]. However, icosahedral nuclei have rarely been observed in Mg–Zn–RE alloys even though the IQC phase is easily formed in these alloys. The main reason for the rarity of the icosahedral nuclei is likely the poor glass-forming ability of the Mg–Zn–RE glass. In the TEM image, similar icosahedral nuclei were found in the zone of the amorphous phase in the RS ribbon, as shown in Fig. 3(b). A number of nanosized IQC particles are likely transformed from the amorphous phase. The results also indicate that the formation of the petal-like IQC phase is more likely diffusion controlled than nucleation controlled in the RS process. These results also coincide with the observation that the longer holding time promotes the formation of the block-shaped IQC phase at the liquid temperature [23].

Additional stable IQC phases have been found and studied systematically, especially for the icosahedral phase based on Mg–Zn–RE [8,15]. However, most of the IQC phases based on Mg–Zn–RE are well known to be metastable or even unstable at temperatures greater than 400°C [7,16]. This kind of phase could transform to the W phase (400°C), H phase (415°C), or F phase [17–18], among others. In the present work, the icosahedral phase based on Mg–Zn–Gd was stable during the heat treatment process at 200–300°C but changed to a hexagonal phase (μ-phase) when the ribbons were heat-treated at 400°C for 0.5 h, as shown in Figs. 4(a) and 5(b). Figs. 5(d) and 5(e) display the corresponding SAED patterns. The short-rod-shaped μ-phase with a composition of $Mg_{31.6}Zn_{61.8}Gd_{7.1}$ (Fig. 4(a)) plentifully precipitated on the Mg matrix. This phase contains more Zn atoms and fewer Mg atoms than the α-Mg matrix. Even so, the heat treatment had little effect on the morphology of the H1 phase at 400°C. The chemical composition of the H1 phase exhibited a slight change to $Mg_{29}Zn_{59}Gd_{12}$ during the heat treatment. Although the composition of the μ-phase is quite similar to that of the H1 phase, the lattice parameters of these two phases substantially differ. The crystal structure of the μ-phase and H1 phase were determined to be hexagonal type, with a = 1.415 nm, c = 0.908 nm and a = 2.107 nm, c = 0.795 nm, respectively, as obtained from Figs. 5(c)–5(e). Fig. 4(b) shows that the μ-phase grows and coarsens during non-isothermal treatment at 400°C, resulting in particles larger than those formed during the isothermal heat treatment. Figs. 5(a)–5(b) show the corresponding TEM images of the H1 phase and the μ-phase in the heat-treated RS alloy, respectively. The block-shaped H1 phase grew slightly during the heat treatment process, and the newly formed μ-phase has a regular hexagonal morphology with several micrometers in the transversal surface.

According to Sugiyama *et al*. [25], the short-rod-shaped μ-phase with the composition $Mg_{28.6}Zn_{63.8}Gd_{7.7}$, as the crystalline approximant of the IQC phase, was also observed in the as-cast $Mg_{42}Zn_{50}Gd_8$ alloy after annealing at 540°C for 20 h. In the present work, the results clearly indicate that the μ-phase could also rapidly form at the expense of the nanosized IQC phase under a lower-temperature (400°C for 0.5 h) heat treatment, although it is still seldom found after treatment at 400°C for 0.2 h. We speculate that the formation of the μ-phase is controlled by its growth rather than by its nucleation. The crystal structure of the μ-phase [25] shows that this phase includes seven Zn atomic sites and that these Zn atoms are described as icosahedra with 12 nearest neighbors. These Zn atoms can be directly supported by the IQC phase. Consequently, the μ-phase can conveniently nucleate without long-range atomic diffusion under high-temperature conditions because its chemical composition is similar to that of the IQC phase.

3.2. Micromechanical properties of the phases

The section details the results of nanoindentation analyses conducted at two temperatures (25 and 400°C). Fig. 6(a) shows the load–depth curves of the IQC phase, μ-phase, H1

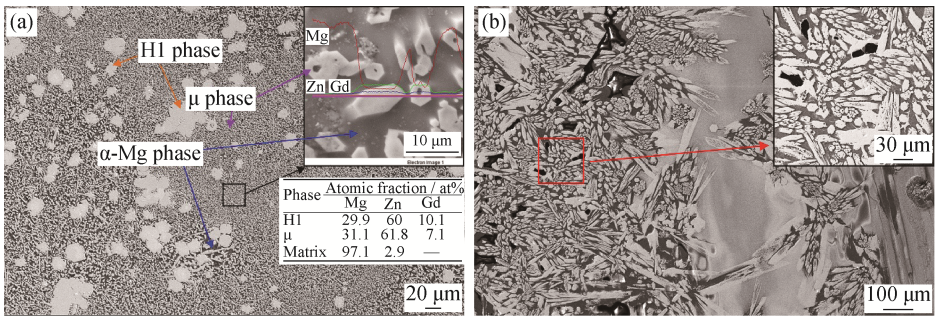

Fig. 4. SEM microstructure of the thicker RS ribbons after heat treatment: (a) isothermal heat treatment at 400°C; (b) non-isothermal heat treatment at 400°C. The insets in (a) show the scanning EDS through the μ-phase and α-Mg matrix and the average EDS analysis results of the phases.

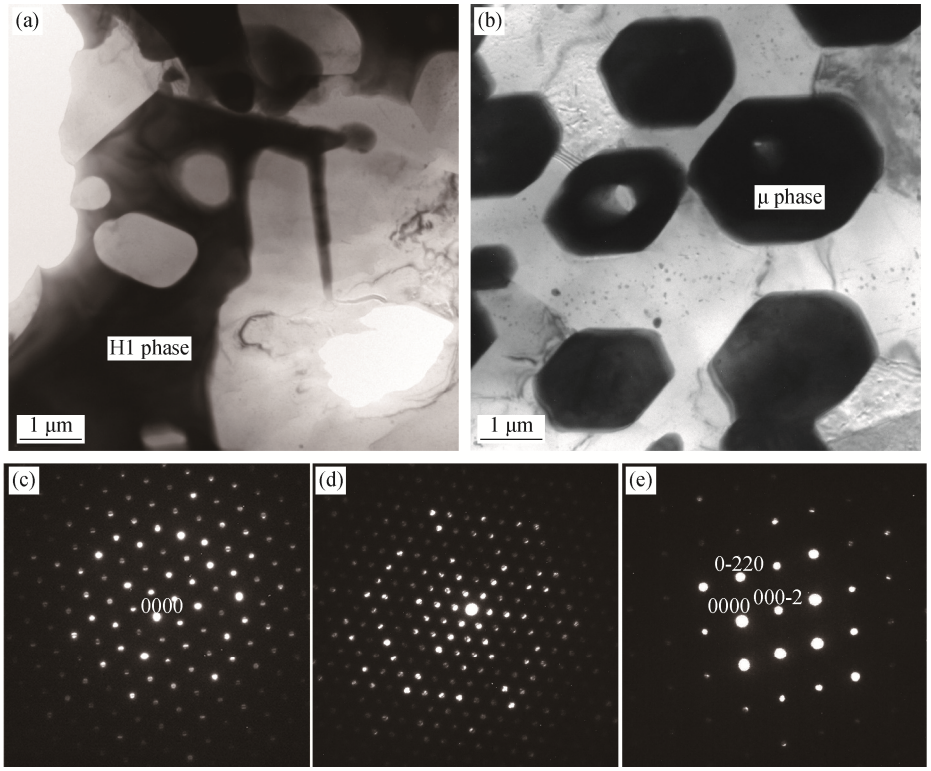

Fig. 5. TEM images and SAED patterns of the hexagonal phases after isothermal heat treatment at 400°C in the thicker RS ribbons: (a) bright-field (BF) TEM image of the H1 phase; (b) BF TEM image of the μ-phase; (c) SAED patterns of the H1 phase, where the incident beams are parallel to [0001]; (d, e) SAED patterns of the μ-phase, where the incident beams are parallel to [0001] and [1000], respectively.

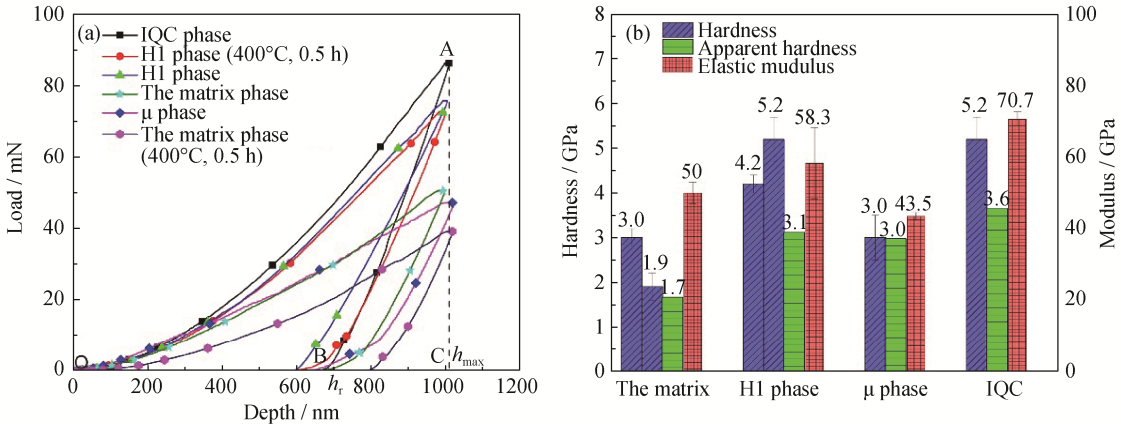

Fig. 6. Micromechanical properties of the RS $Mg_{61.7}Zn_{34}Gd_{4.3}$ alloy based on nanoindentation tests: (a) the load–depth curves of various phases; (b) the hardness (including the apparent hardness after heat treatment) and the Young's modulus of the corresponding phases (HT means heat treatment at 400°C).

phase, and the α-Mg matrix. Notably, the nanoindentation method used in this work was unable to measure the hardness of the isolated nanosized IQC particles or the small zone of the amorphous phase shown in Fig. 3; it instead measured the hardness of the nanosized features within a surrounding amorphous phase and therefore yielded a "mixed" hardness value of the α-Mg matrix with these two phases.

The measured hardness (based on the Oliver-Pharr method) and the Young's modulus of the various phases are summarized in Fig. 6(b). The hardness of the α-Mg matrix is 3.0 ± 0.2 GPa, which includes both the nanosized IQC phase and the amorphous phase. After heat treatment at 400°C, the hardness of the α-Mg matrix decreases to ~1.9 GPa because

fewer solute Zn and Gd atoms are distributed in the solid solution. In the meantime, the nano-IQC phase transforms to the μ-phase, which weakens the α-Mg matrix. The hardness of the H1 phase increases from ~4.2 GPa to ~5.2 GPa after heat treatment. Atomic diffusion occurs during the heat treatment process. Thus, the higher hardness values were obtained because the chemical composition was more uniform and the structure was more stable than those before the heat treatment. The hardness of the μ-phase is taken from the coarse particles; its value, 3.0 ± 0.5 GPa, is similar to that of the matrix containing the nanosized IQC phase and the amorphous phase. The IQC phase exhibits the highest hardness (5.2 ± 0.2 GPa) among these phases.

The apparent hardness (Fig. 6(b)), which is the hardness usually associated with the analysis of the unloading curve [21], was obtained at the same time. The apparent hardness value can be obtained via nanoindentation elastic–plastic deformation theory. Energy is lost as heat during plastic deformation and as stored elastic energy (from residual stresses) within the tested material, which is represented by the net area enclosed by the loading and unloading displacement response [21]. For example, for the IQC phase, the plastic-deformation energy U_p lost is obtained from the area of OAB (Fig. 6(a)) within the load–depth zone. When the values of the maximum load (P_{max}) and indentation depth h (including h_{max} and h_r) are obtained, then the apparent hardness (H_a) can be assessed from Eq. (1):

$$H_a = \frac{U_p}{V_r} \tag{1}$$

where the value of U_p can be calculated by integrating P with respect to h on the basis of the load–depth curve; V_r is the volume of the indentation and is obtained from Eq. (2) on the basis of the residual impression:

$$V_r = \frac{\pi}{3} \cdot (\tan\alpha \cdot h_{max})^2 \cdot h_r \tag{2}$$

where α is the effective cone angle (radians), which is 70.3° in the case of a Berkovich indenter.

The apparent hardnesses of all of the phases are obviously smaller than the hardnesses obtained via the Oliver–Pharr method (Fig. 6(b)). This discrepancy suggests that these phases exhibit elastic–plastic deformation—specifically, these phases represent the resistance to both elastic and plastic deformations, not just the resistance to plastic deformation. Although the hardness of the H1 phase is equal to that of the IQC phase, the apparent hardness of the latter (~3.6 GPa) is greater than that of the former (~3.1 GPa), implying that the IQC phase could endure greater deformation resistance, mainly because of the high elastic modulus of the IQC phase.

The modulus of the α-Mg matrix and the μ-phase are similar and approach that of the pure Mg (~44 GPa). The IQC phase exhibits the highest elastic modulus among these phases; its value is approximately 70.7 GPa. Fig. 7 shows SEM images of the indentations on these phases. Fig. 7(a) shows the indentations of the α-Mg matrix containing fine short-rod-shaped μ-phase after the heat treatment. Notably, the deformational zone does not appear around this indentation and the same behavior is also observed on the coarse μ-phase, as shown in Fig. 7(c). The hardness of the H1 phase is uncertain and might be greater than the actual value because pile-up deformation substantially occurs around the indentation of the H1 phase, as evident in Fig. 7(b). This observation implies that the H1 phase is likely a non-strain-hardening material with a high value of E/σ_y (where E is the elastic modulus and σ_y denotes the yield stress) [21]. That is, this phase will exhibit a low yield stress under the tensile load condition. A similar phenomenon is also observed near the zone of the IQC phase, as shown in Fig. 7(d). Pile-up occurs only in a very small zone around the edges of the indentation of this phase. Therefore, its effect can be ignored for the IQC phase. The highest hardness is observed in the petal-shaped IQC phase. The hardness of the hexagonal H1 phase is substantially greater than that of the μ-phase with the same structure, possibly because the H1 crystal structure contains more Gd atoms.

The plasticity index, ψ, is a parameter that characterizes the relative plastic/elastic behavior of a material subjected to external stresses [18]. In the case of indentation contacts, the value of ψ is obtained from Eq. (3) on the basis of the energy method [19,21]:

$$\psi = \frac{U_p}{U_e + U_p} \tag{3}$$

where the elastic-deformation energy U_e lost is obtained from the area of the elastic zone, similar to the area of *ABC* for the IQC phase.

Fig. 8 displays the plasticity index (ψ) of the four phases. The values of ψ for the IQC and H1 phases are smaller than those of the Mg matrix and the μ-phase. These results imply that the two former phases resist elastic deformation better than the latter two phases. These observations are consistent with the trends of the corresponding high elastic modulus. The values of ψ for the μ-rod and α-Mg matrix phases are similar because the sizes of the μ-phase are relatively small; thus, the tested indentation might permeate into the solid-solution matrix phase (α-Mg). The results also indicate that less plastic deformation occurs in the H1 phase than in the IQC phase.

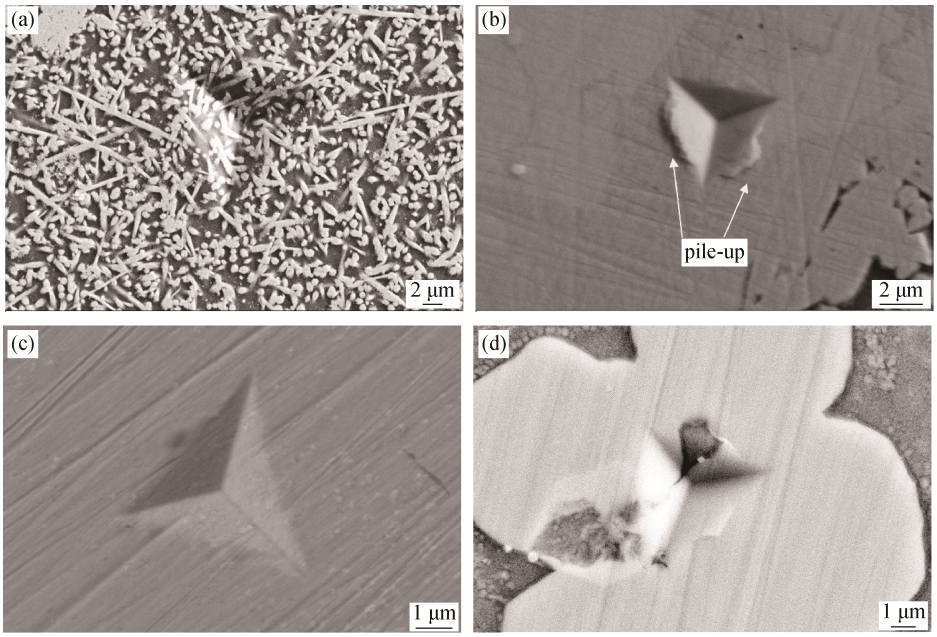

Fig. 7. SEM images of the indentations: (a) the matrix and nano-size μ-phase in the thicker ribbons after heat treatment at 400°C for 0.5 h; (b) the H1 phase in the as-sprayed thicker ribbons; (c) the block-shaped μ-phase in the thicker ribbons after heat treatment at 400°C for 0.5 h; (d) the petal-shaped IQC phase in the as-sprayed thicker ribbons.

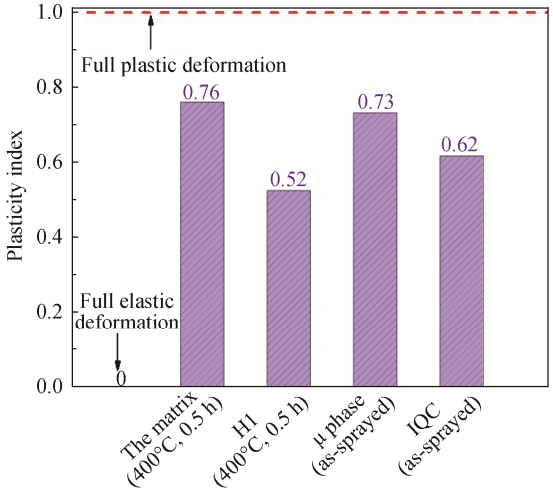

Fig. 8. Plasticity indexes of various phases in the as-sprayed thicker $Mg_{61.7}Zn_{34}Gd_{4.3}$ ribbons or the ribbons after heat treatment at 400°C for 0.5 h.

4. Conclusions

The effect of heat treatment on the microstructures and mechanical properties of the RS $Mg_{61.7}Zn_{34}Gd_{4.3}$ (at%) alloy were studied in detail. The following conclusions were drawn:

(1) The phases in the thick RS ribbons consist of petal-like IQC phase (~20 μm) with a P-type structure and block-like H1 phase (~15 μm) with a hexagonal structure. However, the IQC particles with an average grain size of ~107 nm, as well as a small proportion of amorphous phase, are found in the thinner RS ribbons.

(2) The IQC phase generally transforms to a short-rod-liked μ-phase with the hexagonal structure and a composition of $Mg_{28.6}Zn_{63.8}Gd_{7.7}$ during heat treatment at 400°C for 0.5 h. Meanwhile, the H1 phase with the composition of $Mg_{26\text{-}30}Zn_{56\text{-}60}Gd_{10\text{-}14}$ grows slightly during this process.

(3) The hardness values of the α-Mg matrix, block-like H1 phase, short-rod-like μ-phase, and petal-shaped IQC phase are 3.0 ± 0.2 GPa, 4.2 ± 0.2 GPa, 3.0 ± 0.5 GPa, and 5.2 ± 0.5 GPa, respectively. The hardness of the H1 phase is similar to that of the IQC phase after heat treatment at 400°C. Additionally, the IQC phase exhibits the highest apparent hardness among these phases.

(4) The IQC phase and H1 phase exhibit a lower plasticity index than the α-Mg matrix because of their higher elastic modulus. The H1 phase exhibits poorer plastic behavior than the IQC phase but a higher elastic modulus than the α-Mg matrix.

Acknowledgements

This work is supported by the Youth Science Fund Project of National Natural Science Fund of China (No. 51401070). We also gratefully acknowledge Dr. Li You from University of Science and Technology Beijing for the discussion of TEM results' analysis.

References

[1] F.C.T, Alloys of magnesium, *Nature*, 141(1938), p. 45.

[2] J.D. Robson, Critical assessment 9: Wrought magnesium alloys, *Mater. Sci. Technol.*, 31(2015), No. 3, p. 257.

[3] B.L. Mordike and T. Ebert, Magnesium: properties-applications-potential, *Mater. Sci. Eng. A*, 302(2001), No. 1, p. 37.

[4] S. Amani and G. Faraji, Recrystallization and mechanical properties of WE43 magnesium alloy processed via cyclic expansion extrusion, *Int. J. Miner. Metall. Mater.*, 25(2018), No. 6, p. 672.

[5] N. Tahreen and D.L. Chen, A critical review of Mg–Zn–Y Series alloys containing I, W, and LPSO phases, *Adv. Eng. Mater*., 18(2016), No. 12, p. 1983.

[6] L. Zhang, Z. Liu, and P.L. Mao, Effect of annealing on the microstructure and mechanical properties of Mg–2.5Zn–0.5Y alloy, *Int. J. Miner. Metall. Mater.*, 21(2014), No. 8, p. 779.

[7] D.V. Louzguine-Luzgin and A. Inoue, Formation and properties of quasicrystals, *Annu. Rev. Mater. Res.*, 38(2008), p. 403.

[8] A.P. Tsai, A. Niikura, A. Inoue, T. Masumoto, Y. Nishida, K. Tsuda, and M. Tanaka, Highly ordered structure of icosahedral quasicrystals in Zn–Mg–RE (RE ≡ rare earth metals) systems, *Philos. Mag. Lett.* 70(1994), No. 3, p. 169.

[9] S. Ranganathan and K. Chattopadhyay, Quasicrystals, *Annu. Rev. Mater. Res.*, 21(1991), No. 1, p. 437.

[10] W.A. Cassada, Y. Shen, S.J. Poon, and G.J. Shiflet, $Mg_{32}(Zn Al)_{49}$-type icosahedral quasicrystals formed by solid state reaction and rapid solidification, *Phys. Rev. B*, 34(1986), No. 10-15, p. 7413.

[11] D.H. Bae, S.H. Kim, D.H. Kim, and W.T. Kim, Deformation behavior of Mg–Zn–Y alloys reinforced by icosahedral quasicrystalline particles, *Acta Mater.*, 50(2002), No. 9, p. 2343.

[12] D.K. Xu, T.T. Zu, M. Yin, Y.B. Xu, and E.H. Han, Mechanical properties of the icosahedral phase reinforced duplex Mg–Li alloy both at room and elevated temperatures, *J. Alloys Compd*., 582(2014), p. 161.

[13] A. Singh, M. Nakamura, M. Watanabe, A. Kato, and A.P. Tsai, Quasicrystal strengthened Mg–Zn–Y alloys by extrusion, *Scripta Mater.*, 49(2003), No. 5, p. 417.

[14] X.D. Wang, W.B. Du, Z.H. Wang, K. Liu, and S.B. Li, Microstructures and mechanical properties of quasicrystal reinforced AZ31 matrix composites, *Mater. Sci. Eng. A*, 530(2011), p. 446.

[15] A.P. Tsai, Discovery of stable icosahedral quasicrystals: progress in understanding structure and properties, *Chem. Soc. Rev.*, 42(2013), No. 12, p. 5352.

[16] J. Gröbner, A. Kozlov, X.Y. Fang, S.M. Zhu, J.F. Nie, M.A. Gibson, and R. Schmid-Fetzer, Phase equilibria and transformations in ternary Mg–Gd–Zn alloys, *Acta Mater.*, 90(2015), p. 400.

[17] J.F. Liu, Z.Q. Yang, and H.Q. Ye, In situ transmission electron microscopy investigation of quasicrystal-crystal transformations in Mg–Zn–Y alloys, *J. Alloys Compd.*, 621(2015), p. 179.

[18] S.V. Ketov, Y.H. Sun, S. Nachum, Z. Lu, A. Checchi, A.R. Beraldin, H.Y. Bai, W.H. Wang, D.V. Louzguine-Luzgin, M.A. Carpenter, and A.L. Greer, Rejuvenation of metallic glasses by non-affine thermal strain, *Nature*, 524(2015), No. 7564, p. 200.

[19] Y.N. Wang, J. Yang, and Y.P. Bao, Effects of non-metallic inclusions on machinability of free-cutting steels investigated by nano-indentation measurement, *Metall. Mater. Trans. A*, 46(2015), No. 1, p. 281.

[20] A. Rahnama, H. Kotadia, S. Clark, V. Janik, and S. Sridhar, Nano-mechanical properties of Fe–Mn–Al–C lightweight steels, *Sci. Rep.*, 8(2018), art. No. 9065.

[21] A.C. Fisher-Cripps, *Nanoidentation*, Springer, New York, 2012, p. 60.

[22] R. Yang, Q. Zhang, P. Xiao, J. Wang, and Y.L. Bai, Two opposite size effects of hardness at real nano-scale and their distinct origins, *Sci. Rep*., 7(2017), art. No. 10653.

[23] J.Y. Zhang, P. Jia, D.G. Zhao, G.R. Zhou, and X.Y. Teng, Melt holding time as an important factor on the formation of quasicrystal phase in $Mg_{67}Zn_{30}Gd_3$ alloy, *Physica B*, 533(2018), p. 28.

[24] D.B. Miracle, A structural model for metallic glasses, *Nat. Mater.*, 3(2004), No. 10, p. 697.

[25] K. Sugiyama, K. Yasuda, T. Ohsuna, and K. Hiraga, The structures of hexagonal phases in Mg–Zn–RE (RE = Sm and Gd) alloys, *Z. Kristallogr.*, 213(1998), No. 10, p. 537.